JOURNAL OF PROPULSION AND POWER
Vol. 19, No. 5, September–October 2003

Numerical Parameter Studies of Ion-Thruster-Beam Neutralization

Carsten Othmer* and Karl-Heinz Glassmeier†
Institut für Geophysik und Meteorologie, 38106 Braunschweig, Germany
Uwe Motschmann‡
Institut für Theoretische Physik, 38106 Braunschweig, Germany
and
Ingo Richter§
Institut für Geophysik und Meteorologie, 38106 Braunschweig, Germany

Ion-thruster-beam neutralization is an essential process of the operation of ion engines. By means of a three-dimensional electromagnetic particle-in-cell simulation, we carry out parameter studies of the basic plasma physics underlying this process. Special emphasis is paid to the role of the injection velocity ratio between electron thermal velocity and ion bulk velocity. For the dependence of beam quantities such as electron temperature and beam potential on the injection velocity ratio, we derive scaling laws, which are shown to be in good agreement with measurements taken aboard the Deep Space 1 spacecraft. In particular, the experimentally observed discrepancy between electron temperature and beam potential is reproduced by our simulations and is found to be caused by a quasi-Fermi-deceleration of the electrons at the boundaries of the expanding ion beam.

Nomenclature

b	=	ion beam diameter
c	=	vacuum velocity of light
D	=	spring constant
$\mathrm{d}\boldsymbol{A}$	=	area element
$\boldsymbol{E}$	=	electric field vector
e	=	elementary charge ($e > 0$)
F	=	force
f	=	electron distribution function
k_B	=	Boltzmann constant
l_e	=	c/ω_{pe}^0, electron inertia length
m_e	=	electron mass
n_e	=	electron density
n_i	=	ion density
n_{i0}	=	ion density close to the injection plane
Q	=	total electric charge
R	=	beam radius
r	=	radial coordinate
T_e	=	electron temperature
T_{e0}	=	electron temperature upon injection
T_i	=	ion temperature
t	=	time
v_{av}	=	average velocity among forward-streaming and reflected electrons
v_e	=	electron velocity
v_e^{th}	=	electron thermal velocity
v_{e0}^{th}	=	electron thermal velocity upon injection
v_{i0}	=	ion bulk velocity upon injection
v_{refl}	=	velocity of reflected electrons
v_x, v_y, v_z	=	electron velocity components
$\hat{v}$	=	v_x/v_{e0}^{th}, normalized axial velocity
Δt	=	time-step length
Δx	=	grid spacing
$\Delta\Phi$	=	$\Phi_{\mathrm{beam}} - \Phi_{\mathrm{loc}}$, potential difference
ε_0	=	electric vacuum permittivity
η	=	$v_{e0}^{\mathrm{th}}/v_{i0}$, injection velocity ratio
η_{crit}	=	critical injection velocity ratio
κ	=	$1 - n_e/n_i$, degree of nonneutrality
κ_{OB}	=	κ as determined from outboard magnetometer measurements
$\kappa_{\Delta\Phi}$	=	κ as determined from potential measurements
λ_D	=	Debye length
ρ	=	charge density
τ	=	oscillation period of meandering movement
Φ	=	electric potential
Φ_{beam}	=	potential inside the ion beam
Φ_{loc}	=	local potential at Langmuir probe
Φ_{sc}	=	spacecraft ground potential
Φ_0	=	$k_B T_{e0}/e$, electric potential corresponding to electron thermal energy
ω	=	oscillation period of meandering movement
ω_{pe}^0	=	electron plasma frequency for $n_e = n_{i0}$

Received 23 August 2001; revision received 11 March 2003; accepted for publication 9 May 2003. Copyright © 2003 by the authors. Published by the American Institute of Aeronautics and Astronautics, Inc., with permission. Copies of this paper may be made for personal or internal use, on condition that the copier pay the $10.00 per-copy fee to the Copyright Clearance Center, Inc., 222 Rosewood Drive, Danvers, MA 01923; include the code 0748-4658/03 $10.00 in correspondence with the CCC.

*Research Assistant, Mendelssohnstr. 3.
†Professor, Mendelssohnstr. 3.
‡Professor, Mendelssohnstr. 3.
§Associate Professor, Mendelssohnstr. 3.

I. Introduction

ELECTRIC-PROPULSION devices are valued as very efficient forms of space propulsion. Recently, interest in such devices has grown considerably: The Deep Space 1 (DS1) spacecraft of NASA and the European Space Agency's Artemis satellite, which was launched in July 2001, employ ion thrusters for orbit and attitude maneuvers.

These engines derive their thrust from the electrostatic acceleration of xenon ions. Outside the thruster the ejected ions form a dense beam with a characteristic kinetic energy of about 1 keV. For the ion beam to propagate, it needs to be electrically neutralized. For this purpose a hollow cathode, mounted on the thruster periphery, injects electrons into the beam. Apart from that, some unionized neutrals escape from the thruster and—through collisions with energetic beam ions—generate a low-energy charge-exchange plasma plume around the thruster.

The process of neutralization, that is, the mixing of electrons and ions, presents a challenging problem: To neutralize both the ion charge density and the ion current, the electrons being emitted with random velocities from a small cathode on one side of the ion beam have to spread out across the whole beam cross section and also

have to adapt their average velocity to the ion bulk movement. The detailed physics that govern ion-thruster-beam neutralization are only poorly understood. Early treatments of this problem go back to Buneman and Kooyers,[1] Dunn and Ho,[2] and Wadhwa et al.,[3] who carried out one- and two-dimensional computer simulations of the mixing between cold streaming ions and cold or hot electrons. These authors found that self-excited fluctuating space-charge fields at the electron plasma frequency provided the entropy increase needed for a proper mixing of electrons and ions and thus led to the creation of a stable streaming plasma.

Those investigations defined the state of the art in understanding ion-beam neutralization for about 35 years. In a series of recent papers, Othmer et al.[4–6] revisited this problem and started an in-depth analysis of the physics underlying neutralization. Their three-dimensional electromagnetic particle-in-cell (PIC) simulations revealed the governing role of the injection velocity ratio $\eta := v_{e0}^{\text{th}}/v_{i0}$ between the electron thermal velocity and the ion bulk velocity. Depending on the value of η, the overall beam behavior was found to switch between two completely different scenarios: For η being smaller than a critical value η_{crit}, a moving electrostatic shock emerges, which generates a fully thermalized electron component downstream; whereas for $\eta > \eta_{\text{crit}}$, no shock occurs, and the electrons are not thermalized. Such switching was shown also to occur in the presence of an axial magnetic field, for example, by permanent magnets inside the thruster chamber.[6] In all cases the critical injection velocity ratio η_{crit} corresponds to the downstream electron thermal velocity equaling the ion bulk velocity.

Apart from revealing the possibility of a shock-like neutralization, which has never been reported before, the simulations of Othmer et al.[4–6] provided some general insight into the complex process of ion-thruster-beam neutralization and its dependence on injection velocity ratio η, beam diameter, and magnetic field. A major shortcoming of those investigations is, however, the simplification of the simulated geometry to a quasi-one-dimensional configuration. Disregarding the actual spatial separation of electron and ion source, Othmer et al. injected both particle species through a common opening. The present study is therefore dedicated to an investigation of ion-thruster-beam neutralization under full consideration of the spatial separation between the electron and ion sources. The investigation findings are presented as follows. After briefly introducing the simulation setting in the next section, we present a detailed analysis of the electron dynamics for the case $\eta = 1$ in Section III. The injection velocity ratio η as a governing parameter of the neutralization process is further discussed in Section IV, which features simulation results for varying values of η. For the η dependence of basic beam quantities such as degree of nonneutrality, potential and electron temperature, we derive scaling laws, which are shown to be in good agreement with thruster-beam measurements aboard DS1 (Section V).

II. Simulation Setting

For the simulations to be presented in the following, we employ the same three-dimensional electromagnetic, collisionless PIC code as Othmer et al.[4–6] However, in contrast to their quasi-one-dimensional configuration with electrons and ions entering the simulation domain through a common quadratic opening, we now employ a geometry according to Fig. 1: electrons and ions are injected in equal numbers per time step through spatially separated, round orifices. Their diameters are fixed at 3 Debye lengths λ_D (corresponding to 0.2 electron inertia lengths l_e), and $15\lambda_D$ ($1.1l_e$), respectively. The plasma conditions that determine the Debye length are those of a fully neutralized beam, that is, with $n_e = n_{i0}$, and with an electron temperature T_e equal to the injection value T_{e0}. For the actual DS1 thruster λ_D is approximately 2×10^{-4} m (Ref. 4).

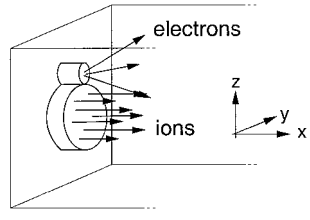

Fig. 1 Simulation geometry with completely separated, round injection areas.

When measured in l_e, the simulated ion-beam diameter is comparable to the DS1 value ($3.75l_e$ or $1500\lambda_D$, Ref. 4). As measured in λ_D, however, we actually simulate a scaled-down version of an ion thruster. To be applied to actual ion engines, our results have to be rescaled appropriately, for example, by matching ratios of characteristic lengths (see Ref. 7 and Section V). The somewhat arbitrary diameter ratio of $\frac{3}{15}$ is determined by numerical constraints: 1) beam diameters of more than $15\lambda_D$ are at present too computationally taxing for our model and 2) the practically point-like electron emitter of the real ion thruster was extended to three grid cells, that is, to $3\lambda_D$, in order to have some spatial resolution of the conditions around the electron orifice.

Characteristic particle velocities for ion engines are $v_{e0}^{\text{th}} = 4 - 9 \times 10^5$ m/s for the thermal velocity of the electrons and $v_{i0} \approx 3.5 \times 10^4$ m/s for the ion bulk velocity.[8] However, the velocity that determines the time-step size in our fully electromagnetic code is the velocity of light of approximately $c = 3 \times 10^8$ m/s. Therefore, in order to accommodate the processes on the timescale of the electron and ion velocities within a reasonable number of time steps the original particle velocities have to be rescaled toward higher values. As it is not the absolute values of the involved velocities but rather their ratio, this should not alter the physics significantly.[4] The thermal velocity of the electrons $v_{e0}^{\text{th}} = \sqrt{(k_B T_{e0}/m_e)}$, which are injected with a half-Maxwellian velocity distribution in v_x and a full-Maxwellian in v_y and v_z, is therefore fixed at $0.1c$ throughout the paper, where c is the velocity of light. Ions leave the injection plane with a bulk velocity v_{i0} plus a small thermal spread corresponding to $T_i = 0.04T_{e0}$ (according to Ref. 7). The velocity ratio $\eta = v_{e0}^{\text{th}}/v_{i0}$ is varied between 1.0 and 8.0 by adjusting v_{i0} correspondingly.

Because of the original electron-to-xenon-ion mass ratio of roughly 1 : 250000, the timescales of the respective particle species are widely separated. A common trick in numerical simulations that allows the coverage of both timescales within the simulation run time is to bring them closer together by increasing the electron-to-ion mass ratio. With such a manipulation the simulation results are quantitatively no longer correct, but—as long as the electron and ion time scales are still separated enough to be distinguished—the model qualitatively represents the characteristics of the simulated system. In this paper, however, we rather use the original mass ratio and focus solely on the high-frequency electron dynamics, as did Othmer et al.[4–6] in their quasi-one-dimensional studies. We run the simulations typically for about $\omega_{\text{pe}}^0 t = 300$, which corresponds to 0.1 ion plasma periods. Therefore, in our simulations the ion dynamics do not play a role at all, apart from their bulk movement that generates the fields with which the electrons interact.

The grid spacing Δx is set equal to the electron Debye length λ_D, and, in order to fulfill the Courant criterion for electromagnetic waves, the time-step length is chosen such that $\Delta t = 0.4\Delta x/c$. The electron plasma frequency in the fully neutralized beam, that is, for $n_e = n_{i0}$, is $\omega_{\text{pe}}^0 \Delta t = 0.027$, leading to an electron inertia length l_e of $l_e = c/\omega_{\text{pe}}^0 = 14\Delta x$. For an assessment of the numerical accuracy of our simulation, we controlled the energy conservation for some specific runs. With the settings just mentioned, energy was found to be conserved to within about 0.2% after $10^4 \Delta t$, which is a tolerable level.

As the densities of the charge-exchange ions and of the ambient solar wind plasma are smaller than the DS1 ion-beam density by a factor of 4×10^3 (see Ref. 8) and 4×10^9, respectively, these two plasma populations do not have a significant impact on the neutralization and are therefore neglected in our simulation. Moreover, for the simulation time span of about 100 electron plasma periods possible particle collisions are too rare to have a significant influence on the particle dynamics. Hence, for these simulation time spans our inherently collisionless code describes the beam behavior correctly. We further note that all physical quantities in the simulation are dimensionless. They are normalized to basic quantities such as the velocity of light c, the electron Debye length λ_D of the fully neutralized beam, and the electron plasma frequency ω_{pe}^0 for $n_e = n_{i0}$.

III. Case $\eta = 1$

This section is devoted to the results of our simulation runs for the case $\eta = 1$. The electric potential, the electron phase space, as well as electron and ion density in the axial direction after $\omega_{pe}^0 t = 200$ are shown in Fig. 2. By this time the thruster beam has expanded from the injection plane at $x = 10$ up to $x = 270$. The potential was computed by integrating the electric field in the axial direction, averaging across the ion beam, and setting $\Phi = 0$ in the injection plane, and is normalized to $\Phi_0 := k_B T_{e0}/e$. The electron and ion densities are "slice densities," that is, $n_e(x)$ and $n_i(x)$ are obtained by counting all particles in the simulation domain slice between x and $x + \Delta x$. The densities are normalized to the nominal ion slice density of a nondiverging beam n_{i0}.

The electron density is in the order of $0.45 n_{i0}$ (Fig. 2, bottom panel), whereas in the corresponding quasi-one-dimensional case it was around $0.8 n_{i0}$ (Ref. 4). This enhanced loss of electrons is a direct consequence of shifting the electron source outside the ion beam: the electrons are now born with a higher potential energy, and thus a larger fraction of them have now enough total energy to escape from the attractive potential of the ion beam. As a result of the high degree of nonneutrality, the beam potential rises to $24\Phi_0$ with respect to the injection plane and to around $52\Phi_0$ with respect to the ambient level (Fig. 2), as compared to $4\Phi_0$ and $10\Phi_0$ for the quasi-one-dimensional case.[4]

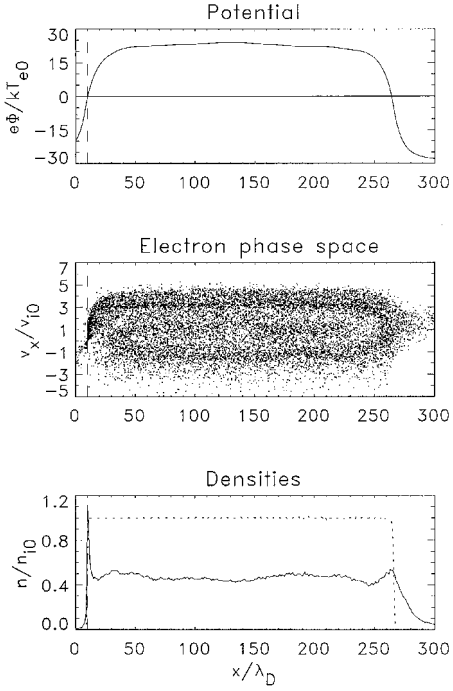

Fig. 2 Axial potential, electron phase space $v_x - x$, and slice densities of electrons (——) and ions (. . . .) for a configuration according to Fig. 1 with $\eta = 1.0$ and $b = 15\lambda_D$. The – – – line indicates the injection plane $x = 10$.

The structure of the potential is that of a reversed potential trough: behind a sharp increase within an injection sheath of roughly $20\lambda_D$ thickness, it remains flat up to the front end of the ion beam where it drops back to the ambient level. In contrast to the corresponding quasi-one-dimensional run for $\eta = 1$, there is no sign of an electrostatic shock.

Despite the strong degree of nonneutrality, there is practically no axial electric field within the beam. Similar to previous observations,[4–6] the electrons arrange themselves in such a manner that the whole electric flux associated with the vast excess of positive charges within the beam emanates through the lateral surfaces.

One of the basic questions of ion-beam neutralization addresses the adaptation of the average electron velocity to the ion bulk movement in the absence of collisions. The electron phase space in Fig. 2 gives a clue on how this is accomplished: the potential increase in the injection sheath accelerates the electrons to form a beam at about $3v_{i0}$. With this velocity the electrons overtake the ions and stream up to the head of the ion beam, where they are reflected. As the head itself is moving at v_{i0}, the inelastically reflected electrons acquire a velocity of $[-(3-1)+1]v_{i0} = -v_{i0}$. They travel back to the stationary injection sheath, where they are again reflected, and end up with a velocity of v_{i0}, that is, they are streaming with the ion bulk velocity.

In other words, after their initial acceleration in the injection sheath the electrons undergo a sort of Fermi deceleration between the expanding ends of the ion beam, which adapts their bulk velocity to v_{i0}. In the simulation run discussed here, this adaptation mechanism seems quite fortunate: just two reflections are needed to provide the electrons with exactly the right velocity. For other situations, where the electrons are not accelerated to roughly $3v_{i0}$ in the injection sheath, this velocity adaptation might not be so effective. More than two reflections between the stationary injection sheath and the moving head of the ion beam might be necessary, and the electrons might not end up with exactly v_{i0}. However, already after a single reflection at the head of the ion beam the electrons streaming with v_e in the $+x$ direction acquire an average velocity among forward streaming and reflected electrons that exactly equals the ion bulk velocity:

$$v_{\text{refl}} = -(v_e - v_{i0}) + v_{i0} \Rightarrow v_{\text{av}} = \tfrac{1}{2}(v_e + v_{\text{refl}}) = v_{i0} \qquad (1)$$

Hence, although being probably not always as effective as in the run of Fig. 2, the quasi-Fermi decelaration represents a universal mechanism of adapting the average electron velocity to the ion bulk movement in the absence of collisions, that is, as long as the distance traveled by the electrons does not significantly exceed their mean free path. Later on, the reflection of electrons at the head of the ion beam becomes increasingly unlikely because electron–ion collisions will tend to diminish any velocity difference between the two particle species. The Fermi deceleration at the head of the ion beam will then become unimportant as a velocity adaptation mechanism and will be replaced by particle collisions.

The three distinct electron beams at $v_x = -v_{i0}$, v_{i0}, and $3v_{i0}$ show up clearly in the velocity distribution function (Fig. 3). The distributions of v_y and v_z are quite similar and represent flattened Maxwellians. The standard deviation of all three velocity

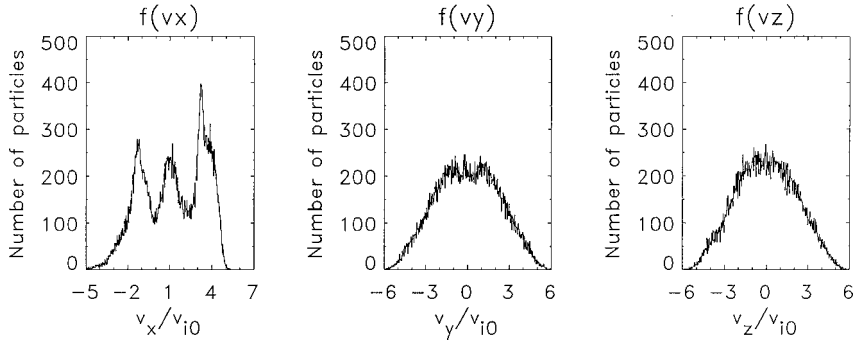

Fig. 3 Three components of the electron velocity distribution function at $x = 220\lambda_D$ for the simulation run of Fig. 2.

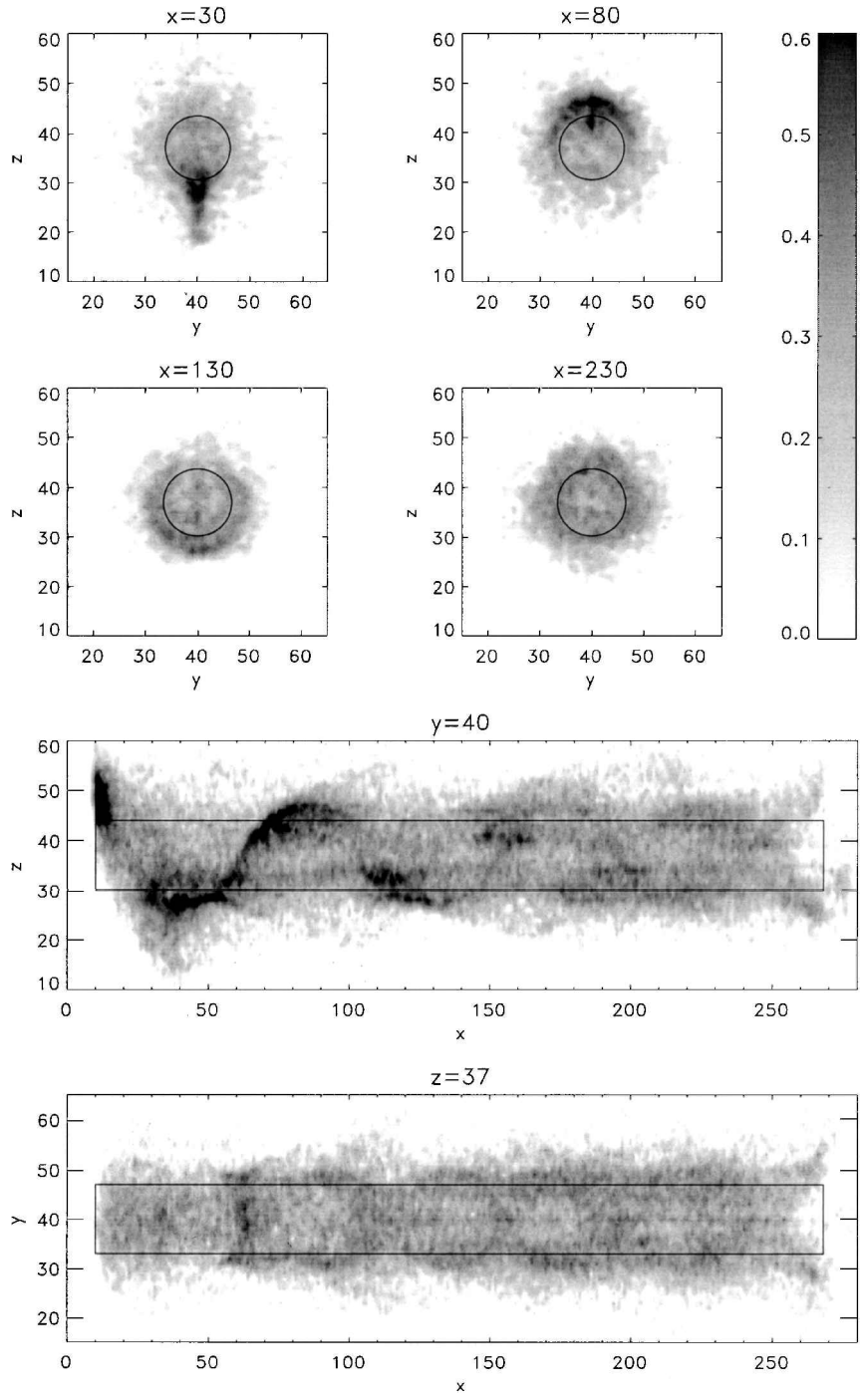

Fig. 4 Electron density cuts for the simulation run of Fig. 2. The coordinates are given in units of λ_D, and the density values are normalized to n_{i0}.

components is roughly $5T_{e0}$ i.e., the electrons here are considerably "hotter" than in the quasi-one-dimensional case[4], where the downstream temperature was around $T_e = 0.35T_{e0}$. The reason for this increase in kinetic energy is again the enhanced potential energy of the electrons upon injection that is associated with the outward shifting of the electron source.

The high electron temperature explains why the potential structure in Fig. 2 does not exhibit such a shock as in the corresponding quasi-one-dimensional case: based on a simple model, Othmer et al.[4] derived a necessary condition for the occurrence of the shock front they observed:

$$v_{i0} > v_e^{\text{th}} \tag{2}$$

that is, the ion-beam velocity must be greater than the electron thermal velocity on the downstream side. The relatively "cold" electrons of the quasi-one-dimensional case with $T_e = 0.35T_{e0}$ fulfilled this condition:

$$v_e^{\text{th}} = v_{e0}^{\text{th}}\sqrt{T_e/T_{e0}} = \eta v_{i0}\sqrt{T_e/T_{e0}} \approx 0.6v_{i0} \tag{3}$$

The high electron temperature in the present run, however, corresponds to $v_e^{\text{th}} = 2.2v_{i0}$ and thus violates Eq. (2). The electrons are simply too hot for a shock-like neutralization to take place.

Figure 4 gives an impression of the three-dimensional behavior of the electrons. It shows contour plots of the electron density for the simulation run of Fig. 2 in four cross sections at $x = 30$, 80, 130, and $230\lambda_D$ as well as in the $x - z$ plane and the $x - y$ plane. The black lines roughly indicate the extent of the ion beam, which, as a consequence of using the actual electron to ion mass ratio of 1:250,000, shows only a slight divergence.

The highest electron density is encountered in front of the electron source, where it amounts to about $1.2n_{i0}$ (exceeding the applied grey scale of Fig. 4; see also Fig. 2). From there, the electrons are accelerated toward the ion-beam center by the attractive potential of the ions. This acceleration takes place within the first 10–20λ_D in axial direction (injection sheath). The electrons overshoot and build up a density enhancement on the opposite side of the beam with a maximum density of about $0.5n_{i0}$. From this region electrons are accelerated back toward the beam center to follow a meandering path between the top and bottom surfaces of the ion beam.

Up to around $x = 70\lambda_D$ or $5l_e$, this path exhibits quite a coherent structure, with the electron density being localized in the central $x - y$ plane. Further downstream, it becomes more diffuse, and the electrons gradually distribute over the whole ion-beam circumference. As can clearly be seen from Fig. 4, the electrons do not fill the beam homogeneously. They concentrate around the ion-beam surface, while the center is practically void of electrons. It is the high kinetic energy gained after falling from the injection plane into the potential trough of the ion beam that makes the electrons circulate around the beam rather than reside in its center.

The wavelength of the meandering path is in the order of $80\lambda_D$ or $5.7l_e$. The meandering path structure can be understood as the superposition of a lateral electron oscillation around the positively charged beam with the electron movement in the $+x$ direction: we consider a single electron at rest on the border of an infinitely long, positively charged cylinder. The electric field of such a cylinder charge can readily be calculated by integrating Gauss' law

$$\int \boldsymbol{E} \cdot \mathrm{d}\boldsymbol{A} = \frac{Q}{\varepsilon_0} \tag{4}$$

which—assuming cylindrical symmetry—yields

$$E(r) = \begin{cases} \dfrac{\rho}{2\varepsilon_0} \cdot r & \text{for} \quad r \le R \\ \dfrac{\rho}{2\varepsilon_0} \cdot \dfrac{R^2}{r} & \text{for} \quad r > R \end{cases} \tag{5}$$

For $r \le R$ the force on the electron is

$$F(r) = -(e\rho/2\varepsilon_0)r =: -Dr \tag{6}$$

with the spring constant D. Hence, the electron will carry out a harmonic oscillation around $r = 0$ with a frequency

$$\omega = \sqrt{\frac{D}{m_e}} = \sqrt{\frac{e\rho}{2\varepsilon_0 m_e}} \tag{7}$$

Introducing the electron plasma frequency of a completely neutralized cylinder

$$\omega_{\mathrm{pe}}^0 = \sqrt{\frac{e^2 n_{i0}}{\varepsilon_0 m_e}} \tag{8}$$

and considering that the charge density of the cylinder is

$$\rho = e(n_{i0} - n_e) \tag{9}$$

where n_{i0} and n_e are the actual ion and electron densities inside the cylinder, the oscillation frequency can be written as

$$\omega = \omega_{\mathrm{pe}}^0 \sqrt{\tfrac{1}{2}(1 - n_e/n_{i0})} \tag{10}$$

The wavelength of the oscillation in the x direction is

$$\lambda = \tau v_x = (2\pi/\omega)v_x \tag{11}$$

We normalize v_x to the electron thermal velocity upon injection

$$\hat{v} := v_x \big/ v_{e0}^{\mathrm{th}} \tag{12}$$

and make use of

$$\omega_{\mathrm{pe}}^0 = \left(1/\sqrt{2}\right)\left(v_{e0}^{\mathrm{th}}/\lambda_D\right) \tag{13}$$

to obtain

$$\lambda = \frac{4\pi\hat{v}}{\sqrt{1 - n_e/n_{i0}}} \cdot \lambda_D \tag{14}$$

The wavelength of the electron oscillation as measured in λ_D depends on the normalized streaming velocity of the injected electrons $\hat{v}$ and the degree of nonneutrality $1 - n_e/n_{i0}$ inside the ion beam.

For the simulation run discussed here, $\hat{v}$ can be taken from Fig. 3 to be around $\hat{v} = 3 \ldots 5$. To compute the degree of nonneutrality inside the beam, the slice density of Fig. 2 is now not the appropriate electron density. We rather have to take the electron density within the ion beam, which was obtained to be around $n_e \approx 0.25n_{i0}$ (not shown), giving a degree of nonneutrality of $1 - n_e/n_{i0} \approx 0.75$. Substituting these values into Eq. (14) yields a wavelength of about $58\lambda_D$, as compared to $80\lambda_D$ in the simulation. Considering that Eq. (14) for the oscillation wavelength is based on a rather simple model, this correspondence is quite good and confirms that the meandering electron path can indeed be understood as the superposition of the axial electron movement with an oscillation around the positively charged beam.

IV. Dependence on Velocity Ratio η

For quasi-one-dimensional configurations the injection velocity ratio $\eta = v_{e0}^{\mathrm{th}}/v_{i0}$ was already identified as a crucial parameter for the overall beam behavior.[4–6] To assess its impact in the case of fully separated particle sources, we carried out three simulation runs similar to the one of the preceding section (from now on referred to as run 1), but with $\eta = 2, 4, 8$ (run 2, 3, and 4) instead of $\eta = 1$. The different injection velocity ratios were realized by keeping the electron thermal velocity fixed at $0.1c$ and varying v_{i0} accordingly. The total simulation time of each run was chosen such that the ion beam reaches roughly the same axial extent by the end of the run. This criterion led to simulation times $\omega_{\mathrm{pe}}^0 t = 200$, 400, 800, and 1600, respectively. To keep the ion density constant, we adapted the number of injected particles per time step according to η. In the following, we will illustrate the η dependence of the overall beam behavior on the basis of the simulation results of runs 2–4. However, for the sake of brevity the display of results is restricted to run 4 (Figs. 5–9), whereas the main outcomes of runs 2 and 3 only appear in Figs. 10 and 11.

The electron density shown in Fig. 5 is again the slice density. The electron density rises from $0.45n_{i0}$ for $\eta = 1$ (Fig. 2) to $0.82n_{i0}$ for $\eta = 8$, meaning that for increasing η the number of electrons with enough total energy to escape from the beam is decreasing significantly. As a consequence of this pronounced η dependence of the neutralization degree, the potential within the ion beam also varies strongly with η (Figs. 2 and 4). With respect to the ambient level, the potential decreases from $52\Phi_0$ in run 1 to $21\Phi_0$ in run 4, thereby following quite well a power law (Fig. 11) according to

$$\Phi/\Phi_0 = 51 \cdot \eta^{-0.43} \tag{15}$$

The global structure of the potential field is still that of a reversed, three-dimensional potential trough. In runs 3 and 4, however, the trough "depth" was found to decrease along the axial direction (Fig. 5) as a result of the decrease of the ion density in the x direction (Fig. 10) that goes along with the lateral expansion of the ion beam: Of course, the beam also expands laterally in runs 1 and 2. Within the shorter simulation times of these runs, however, the expansion is not significant.

The electron phase space for runs 2–4 (Fig. 5) is filled much more homogeneously than that for run 1, where three distinct electron beams were identifiable, and the downstream distribution function for the axial velocity component $f(v_x)$ is getting flatter for increasing η (left panels of Figs. 3 and 6). In all cases, despite the increasing difference between electron and ion velocity upon injection, the average electron velocity is roughly equal to the ion bulk velocity. In

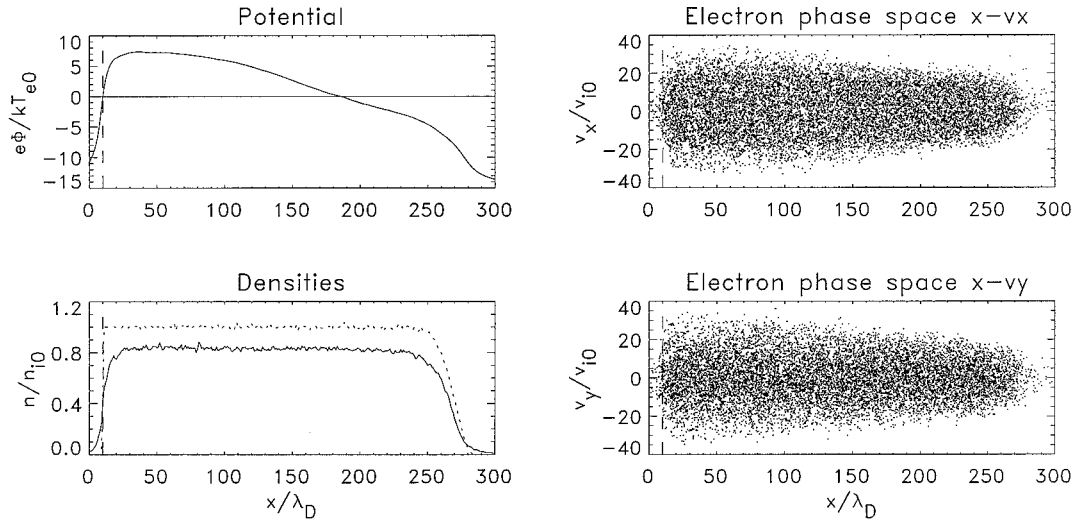

Fig. 5 Axial potential, electron phase space, and slice densities of electrons (——) and ions (. . . .) for $\eta = 8.0$.

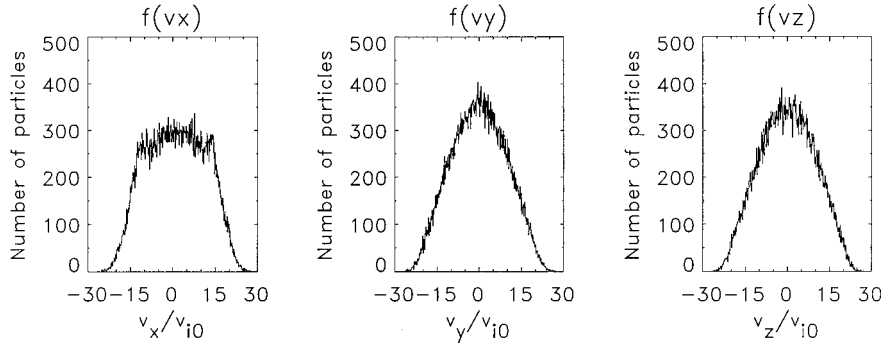

Fig. 6 Three components of the electron velocity distribution function at $x = 220\lambda_D$ for $\eta = 8$.

run 1 a sort of Fermi deceleration was found to be responsible for this velocity adaptation. There is no reason to assume that this process should not be at work also in the other runs. However, it does not show up in the $v_x - x$ phase space as obviously as in run 1. In simulation run 4 we therefore traced a series of electrons from their injection up to the end. The general pattern of their movement in the $v_x - x$ phase space is similar to the one shown in Fig. 8. Through multiple reflections between the moving head of the ion beam and the injection sheath, the electrons indeed adapt their velocity to the ion bulk movement.

Right after its injection, the electron of Fig. 8 gains a maximum velocity v_x of $21 v_{i0}$ and, after a total of seven reflections at the head of the ion beam, its maximum velocity is around $8 v_{i0}$ (bottom panel of Fig. 8). This process amounts to an average absolute velocity change per reflection of $1.6 v_{i0}$, which is quite close to the theoretical value $2 v_{i0}$ for a reflection at a wall moving at v_{i0}. This result suggests that the Fermi-deceleration mechanism is at work also in the case of $\eta > 1$.

In general, the velocity change per reflection shows up in the distribution function $f(v_x)$ as the separation of electron beams that arise through multiple reflections. Hence, with a smaller v_{i0} the electron phase space is filled much more smoothly than with a big v_{i0}, which explains the more homogeneous phase space and the flatter distribution of the axial velocities for increasing η, as observed in Figs. 3 and 6.

However, the simple Fermi mechanism with multiple reflections between a stationary wall and one moving at v_{i0} does not give the whole picture of the actual electron deceleration process: As can be seen from the bottom panel of Fig. 8, the electron is not reflected elastically at the injection sheath, but ususally gains some energy there, and at the front end of the ion beam it loses more than $2 v_{i0}$. Moreover, among the phase space traces recorded in run 4 were also such as depicted in Fig. 9, where the electron transitionally gains kinetic energy at both ends before slowing down via the Fermi mechanism. Such accelerations were, however, quite rare. Hence, although our simple model captures the proper trends of the electron deceleration mechanism it cannot explain the details just discussed, which will be investigated in future studies.

We note from the middle panels in Figs. 8 and 9 that the "bouncing" of electrons between the ion-beam boundaries takes place both in the axial and radial directions. Because of the lateral expansion of the ion beam, this radial bouncing is connected with a loss of kinetic energy of the electrons. In other words, a quasi-Fermi deceleration also takes place in the radial direction. In contrast to the axial Fermi deceleration, which is important only in early times when electrons are likely to reach the front end of the ion beam collisionlessly, the radial Fermi process is undergone by each injected electron, and at later times as well. Thus, the radial Fermi process has a strong impact on the energy budget of the electrons, as will be shown at the end of the next section.

The widths of the velocity distributions, that is, the electron temperatures, are directly related to the amount of potential energy that is transformed into kinetic energy upon falling from the injection area into the potential trough of the ion beam. With decreasing trough depths for growing η, the electron temperatures decrease (Fig. 11). A logarithmic regression yields the following power law for the η dependence of the electron temperature (Fig. 11):

$$T_e / T_{e0} = 5.1 \cdot \eta^{-0.3} \tag{16}$$

whereas for runs 1 and 2 the temperatures are essentially constant along the x direction, there is an appreciable axial decrease of T_e in runs 3 and 4 (both in the axial and the radial temperature; see Fig. 5). This is a consequence of the axial potential slope in these runs: The electrons gain potential energy at the cost of their kinetic energy.

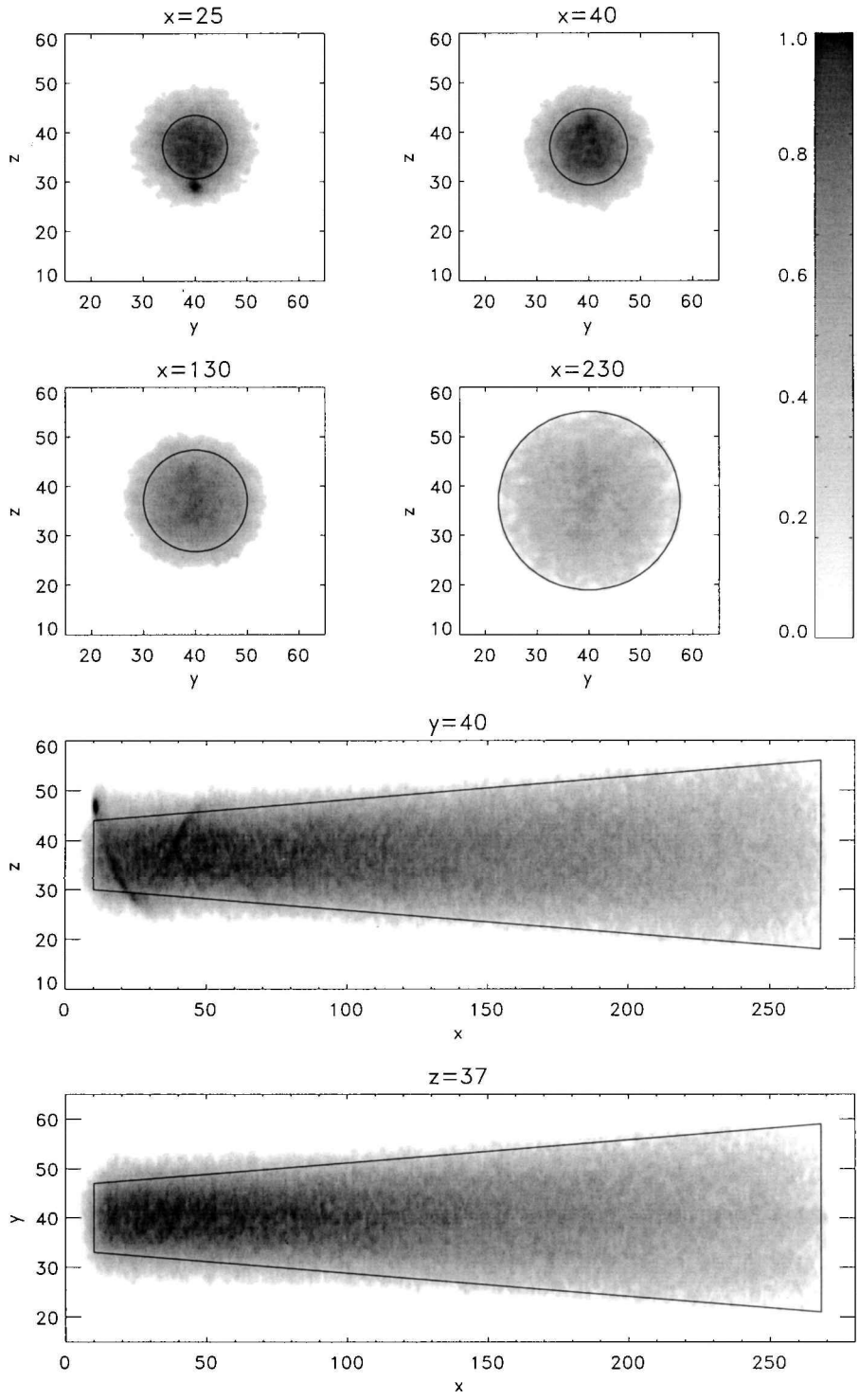

Fig. 7 Electron density cuts for $\eta = 8$.

The three-dimensional distribution of electrons (Figs. 4 and 7) and their flow pattern exhibit a remarkable development from runs 1 to 4. The very structured electron distribution of run 1, which is dominated by the meandering path, is gradually replaced by a rather homogeneous spreading of the electrons over the ion beam. Apparently, the higher frequency of electron reflections at the head of the ion beam associated with an increase of η not only provides a smoother filling of the phase space (see the preceding), but also in physical space.

Even though it does not dominate the electron distribution anymore, the meandering path of the electrons is still visible in runs 2–4. At least $1 + \frac{1}{2}$ oscillations can be traced before the flowfield becomes more turbulent and the density of the meandering electrons disappears in the "background" electron density (Fig. 7). The wavelength λ of the meandering movement decreases for increasing η according to

$$\lambda/\lambda_D = 81 \cdot \eta^{-0.35} \tag{17}$$

As can be seen from Fig. 11, Eq. (14), which is based on quite a simple model, does not reflect the decreasing trend for increasing η very well, but still gives the right order of magnitude for λ.

While in runs 2 and 3, the electrons still tend to avoid the ion-beam center—albeit not as extremely as in run 1 (Fig. 4), the electron density in run 4 actually peaks in the center and decreases radially outward (Fig. 7). In the discussion of run 1 in the preceding section,

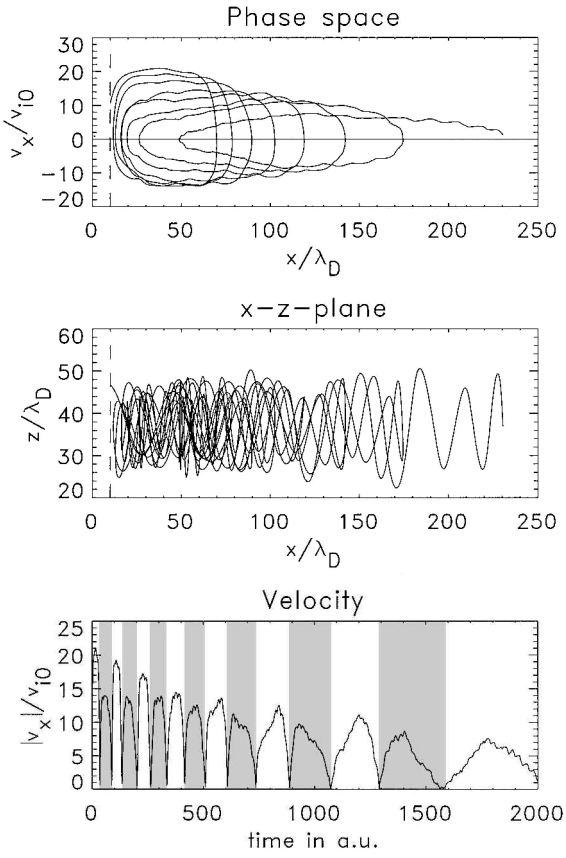

Fig. 8 Dynamics of a representative test electron for $\eta = 8$ (white and grey sections correspond to right-going and left-going legs of the electron path, respectively).

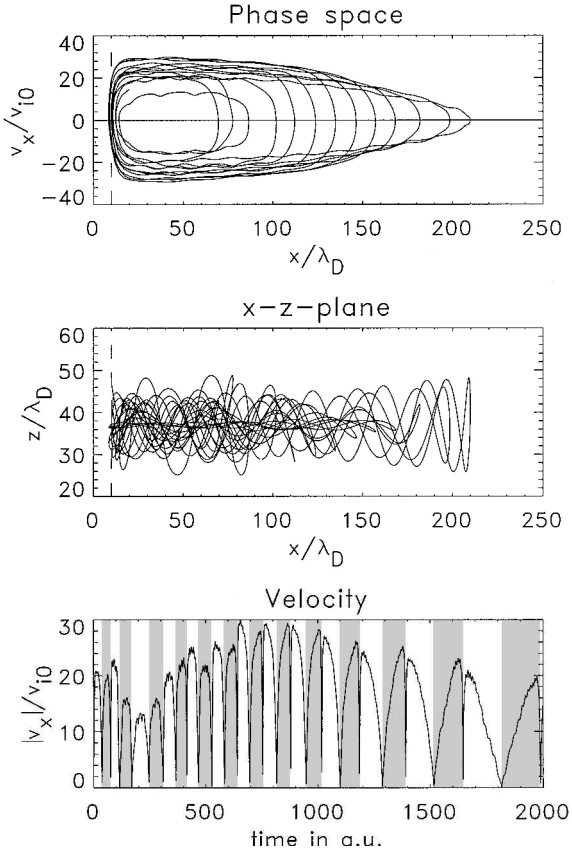

Fig. 9 Same as Fig. 8, but of another, nonrepresentative electron, which transitionally gains kinetic energy in the axial direction.

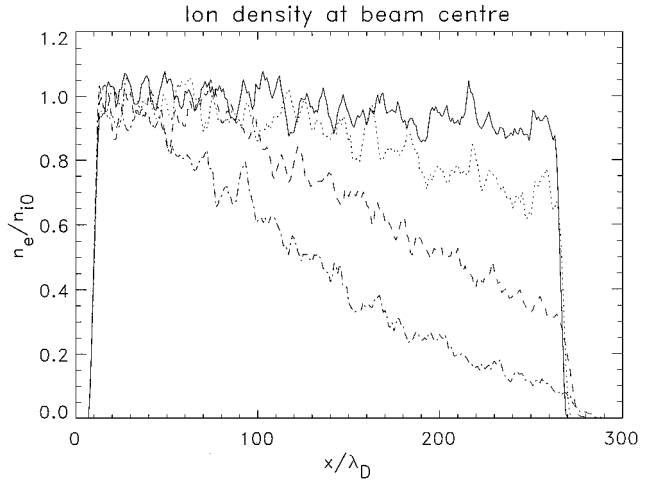

Fig. 10 Ion densities in the center of the beam for $\eta = 1$ (——), 2 (. . . .), 4 (– – –) and 8 (-.-.-).

we explained the observation that the beam center is practically void of electrons with the high kinetic energy of the electrons. These electrons circulate around the beam rather than reside in its center. Because the kinetic energy gained when falling into the potential trough of the ion beam is decreasing for increasing η, the electrons' tendency to avoid the beam center gradually vanishes as η increases.

V. Comparison with DS1 Data

The scaling laws [Eqs. (15–17)] that were obtained from the series of simulation runs of the preceding section reflect the impact of the velocity ratio η on the various beam quantities. Although not being as decisive as in the case of a quasi-one-dimensional geometry,[4,6] η still seems to be an important parameter for the overall beam behavior also in the case of spatially separated particle sources. In general, a higher η leads to a lower degree of nonneutrality, colder electrons, and a lower potential with respect to the ambient. The electron meanders become shorter and less distinct. Whereas T_e, Φ, and λ follow the obtained power laws very well (Fig. 11), the electron density exhibits a more complicated behavior and only slowly approaches a complete neutralization.

Equations (15–17) can be used to extrapolate the plasma parameters toward higher values of η and thus allow a comparison of the simulation results with actual measurements aboard DS1. A quite complete set of DS1 data was recorded during the so-called S-Peak: an operation specifically designed for ion engine diagnostics, where the thruster steps consecutively through three different thrust levels.[8]

The S-Peak operation was started on 22 January 1999 at 21:36 UT and lasted until 22:17 UT of the same day. Among the instruments that collected data during the S-Peak are a Langmuir probe (LP), a retarding potential analyzer (RPA), and the pair of inboard and outboard fluxgate magnetometers (IB, OB). The LP and RPA are colocated at about 0.5 m from the thruster center, while the IB and OB are situated on a boom at a radial distance of 0.8 m and 0.9 m from the thruster center, respectively (Fig. 12).

The LP measures the electron temperature T_e as well as the difference between local potential Φ_{loc} and spacecraft ground Φ_{sc}. The potential of the thruster beam Φ_{beam} relative to spacecraft ground is determined by the RPA from measurements of the kinetic energy of incoming charge exchange (CEX) ions: as these are born cold within the ion beam, their kinetic energy upon reaching the grounded RPA is directly related to $\Phi_{\text{beam}} - \Phi_{\text{sc}}$. Hence, by combining RPA and LP data one can calculate the difference between the local and the beam potential[8]:

$$\Delta\Phi = \Phi_{\text{beam}} - \Phi_{\text{loc}} = (\Phi_{\text{beam}} - \Phi_{\text{sc}}) - (\Phi_{\text{loc}} - \Phi_{\text{sc}}) \qquad (18)$$

$\Delta\Phi$ serves as a proxy for the beam potential with respect to the ambient.

Judging from our simulations, the electrons can be expected to have the same average velocity as the ions. Therefore, any nonneutrality of the thruster beam constitutes an electric current, which

should show up in the OB magnetometer readings (Fig. 12). As the magnetic field signature of such a current is largest in the azimuthal direction, we based our estimate of the nonneutrality $\kappa = 1 - n_e/n_{i0}$ on the azimuthal component of OB. This method is of questionable value, especially in view of the magnetically very disturbed environment of DS1.[9–11]

A more credible way of estimating the degree of nonneutrality is to treat the thruster beam again as an infinitely long, charged cylinder and to use Eq. (5) for the electric field of such a cylinder in order to relate the measured potential difference to the charge density of the beam:

$$\Delta\Phi = \rho R^2 \big/ 4\varepsilon_0 \cdot [1 + 2\ell n(r/R)] \tag{19}$$

Table 1 summarizes the measurements and the derived quantities during the three different thrust intervals of the S-Peak. The values of v_{i0}, n_{i0}, T_e, and $\Delta\Phi$ were provided by Wang et al.,[8] κ_{OB} is computed

Table 1 Measurements and derived beam quantities during the three thrust intervals of the DS1 S-Peak (columns 1, 2, 4, and 5 after Ref. 8)

v_{i0}, km/s	n_{i0}, $10^{15}\mathrm{m}^{-3}$	η	T_e, eV	$\Delta\Phi$, V	κ_{OB}	$\kappa_{\Delta\Phi}$
29.8	1.54	20...28	1.17	9	0.2	$1.7 \cdot 10^{-5}$
37.0	1.96	16...23	1.33	9	0.26	$1.3 \cdot 10^{-5}$
38.7	3.22	15...21	2.09	15	0.24	$1.3 \cdot 10^{-5}$

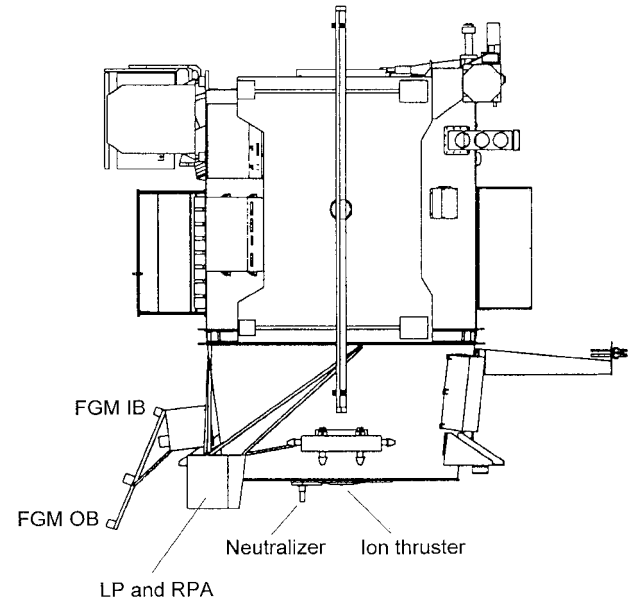

Fig. 12 Side view of the DS1 spacecraft. Note the locations of the fluxgate magnetometers (FGM IB and OB), Langmuir probe (LP), and retarding potential analyzer (RPA).

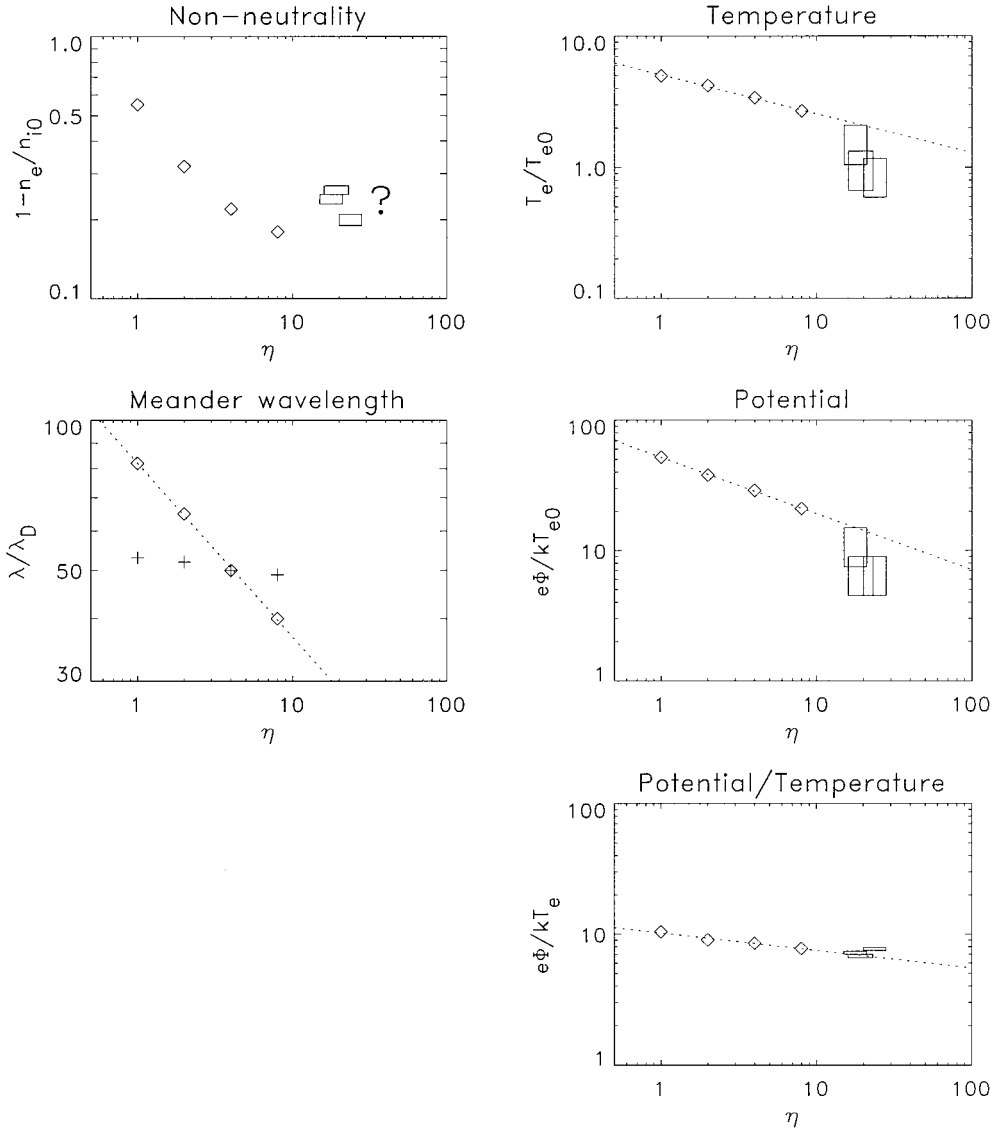

Fig. 11 Dependence on η: ◇, simulation results from runs 1–4; +, meander wavelengths according to Eq. (14); and □, derived values from DS1 data.

from the magnetometer records of Richter,[11] and $\kappa_{\Delta\Phi}$ is calculated from $\Delta\Phi$ as just outlined. The injection velocity ratio η is estimated by assuming an initial electron temperature T_{e0} of 1–2 eV (Ref. 7).

Before comparing them with the results obtained from our simulation, we emphasize that the beam quantities as derived from DS1 measurements are only of a very limited significance. They have been obtained in a rather indirect way, and the quality of the data from which they were derived is quite poor.[8] This is especially true for the magnetic field data.[9–11]

Therefore, the large discrepancy between κ_{OB} and $\kappa_{\Delta\Phi}$ (Table 1) is of no surprise. A nonneutrality of the DS1 beam corresponding to $\kappa_{\mathrm{OB}} = 0.25$ can readily be calculated to lead to lateral expansion velocities vastly exceeding v_{i0} directly behind the thruster exit, that is, to a strong radial divergence of the beam, which is clearly not observed. Hence, as already noted, $\kappa_{\Delta\Phi}$ can be expected to be the more realistic value.

The experimentally derived nonneutrality $\kappa_{\Delta\Phi}$ is much lower than we would expect from an extrapolation of the simulation results ($\approx$0.15, see Fig. 11). Rather than attributing the discrepancy in our results to poor data quality, this disagreement is to be attributed to shortcomings of our simulation: as mentioned in Section II, the simulated ion-beam diameter of $15\lambda_D$ or $1.1l_e$ is comparable to actual ion beams in units of l_e; when measured in λ_D, though, it is scaled down by a factor of about 100. Even though the quasi-one-dimensional simulation results of Othmer et al.[4–6] with shock widths and injection sheath thicknesses all in the range of $1l_e$ suggest the electron inertia length as the governing spatial scale, it might well be that for quantities, such as the nonneutrality, the Debye length λ_D is the relevant length scale. Hence, in order to produce realistic degrees of nonneutrality simulations with greatly enlarged ion-beam diameters are required.

Much larger beam diameters are, however, beyond the present numerical capabilities of our model. But in order to obtain at least the trend on the effects of the beam diameter, we ran a simulation with $\eta = 8$, where we reduced the ion-beam diameter to $7\lambda_D$, that is, to about one-half. Although electron temperature and potential rose only slightly (by roughly 10%) as compared to run 4 (where the beam diameter was $15\lambda_D$), the degree of nonneutrality almost doubled.

Even though this comparison does of course not allow one to derive a quantitative scaling law for an extrapolation toward realistic beam diameters, it clearly exhibits the trend of strongly increasing neutralization with growing beam diameters. The effect of the beam diameter on the beam potential, though, is not as dramatic, because the potential is not only a function of the nonneutrality but rather of the total charge per length, that is, the product of nonneutrality times beam cross section. In other words, smaller beams are less neutral, but also have less charge, such that the beam potential rises only slightly upon decreasing the beam diameter.

Hence, our simulation with a downscaled ion beam tends to overestimate potential and temperature. Having that in mind, one concludes from Fig. 11 that these quantities fit reasonably well with the measurements of Deep Space 1. This conclusion becomes particularly clear when considering the *ratio* between potential and temperature Φ/T_e that partly compensates the overestimating of both quantities: it is almost perfectly consistent with our simulation results (Fig. 11, fifth panel).

The fact that the ratio Φ/T_e stays quite constant, while Φ and T_e themselves drop roughly by an order of magnitude for η ranging from 1 to around 20 (Fig. 11), is a consequence of their close connection: deeper potential troughs provide the electrons with more kinetic energy, that is, with a higher T_e. The proportionality between Φ and T_e does therefore not come as a surprise. What is remarkable, however, is the constant of proportionality: it is in the order of 10, meaning that only about 10% of the electron initial potential energy is converted into kinetic energy. The reason for this startling discrepancy, which has been observed also in other measurements of ion-thruster plumes (Katz, I., private communication, 2001), is the quasi-Fermi deceleration, by virtue of which the electrons lose kinetic energy to the ions. More precisely, the radial Fermi deceleration is the cause of the trends just mentioned because in contrast to axial Fermi deceleration, radial Fermi deceleration continues during stationary thruster operation (see preceding section).

As a result, the ratio between the power values of the scaling laws for potential and temperature, Eqs. (15) and (16), can be explained. Their absolute values, however, as well as the one of Eq. (17) for the meander wavelength are yet to be understood. These three quantities are complex functions of the degree of nonneutrality, which itself was found to have a dependence on η that could not be cast into a simple powerlaw and therefore needs to be addressed in future parameter studies.

VI. Summary

We employed a three-dimensional electromagnetic PIC code for an investigation of the plasma physical processes accompanying ion-thruster-beam neutralization. Refining the quasi-one-dimensional studies of Othmer et al.,[4–6] we considered a more realistic simulation geometry with fully separated electron and ion sources and a practically point-like electron emitter. Special emphasis was paid to the role of the injection velocity ratio $\eta = v_{e0}^{\mathrm{th}}/v_{i0}$ between electron thermal velocity and ion bulk velocity.

Contrary to the simulation results of quasi-one-dimensional geometries, for spatially separated electron and ion sources the thruster beam does not exhibit a shock structure: the electron temperature is too high to fulfill the necessary condition Eq. (2) for shock-like neutralization. Instead, the potential profile rather resembles a featureless reversed potential trough, and the electrons do not adopt a Maxwellian distribution. After their injection the electrons perform a meandering movement between the top and bottom surface of the ion beam before spreading out more homogeneously. A quasi-Fermi deceleration between the expanding ends of the ion beam was found to be responsible for the adaptation of the average electron velocity to the ion bulk movement, as long as collisions are not important, that is, at early times. In the radial direction the Fermi deceleration takes place as a steady-state phenomenon that causes the electrons to lose energy to the ions.

Albeit not as substantially as in the quasi-one-dimensional case,[4,6] the injection velocity ratio η continues to control the electron behavior also for spatially separated particle sources. In general, increasing η results in a higher degree of neutralization, lower beam potentials with respect to the ambient, colder electrons, and a more homogeneous electron distribution within the ion beam. Based on our findings, we derived quantitative relations for the exact dependence of these parameters on η, which—in combination with the available measurements aboard Deep Space 1—give a coherent picture of the impact of η on the overall beam behavior. In particular, the experimentally observed discrepancy between electron temperature and beam potential was confirmed by our simulations and could be attributed to the radial Fermi deceleration of the electrons at the boundaries of the expanding ion beam.

Because of numerical constraints, we simulated a thruster beam with only a small lateral dimension. This was shown to lead to unrealistically high degrees of nonneutrality. We were able to show the qualitative trend on the effect of the beam size by discussing simulation results for a smaller beam diameter, but future studies will have to focus on more realistic beam diameters and on the quantitative impact of the beam diameter on the neutralization process.

References

[1] Buneman, O., and Kooyers, G., "Computer Simulation of the Electron Mixing Mechanism in Ion Propulsion," *AIAA Journal*, Vol. 1, No. 11, 1963, pp. 2525–2528.

[2] Dunn, D. A., and Ho, I. T., "Computer Simulations on Ion-Beam Neutralization with Initially Cold Electrons," *AIAA Journal*, Vol. 1, No. 12, 1963, pp. 2770–2777.

[3] Wadhwa, R. P., Buneman, O., and Brauch, D. F., "Two-Dimensional Computer Experiments on Ion-Beam Neutralization," *AIAA Journal*, Vol. 3, No. 6, 1965, pp. 1076–1081.

[4] Othmer, C., Glassmeier, K. H., Motschmann, U., Schüle, J., and Frick, Ch., "Three-Dimentional Simulations of Ion Thruster Beam Neutralization," *Physics of Plasmas*, Vol. 7, No. 12, 2000, pp. 5242–5251.

[5]Othmer, C., Glassmeier, K. H., Motschmann, U., Schüle, J., and Frick, Ch., "Numerical Simulation of Ion Thruster-Induced Plasma Dynamics," *Advances in Space Research*, Vol. 29, No. 9, 2002, pp. 1357–1362.

[6]Othmer, C., Glassmeier, K. H., Motschmann, U., Schüle, J., and Frick, Ch., "Numerical Simulations on Shock-Like Ion Thruster Neutralization," AIAA Paper 2001-3784, 2001.

[7]Wang, J., Brophy, J., and Brinza, D., "3-D Simulations of NSTAR Ion Thruster Plasma Environment," AIAA Paper 96-3202, 1996.

[8]Wang, J., Brinza, D. E., Young, D. T., Nordholt, J. E., Polk, J. E., Henry, M. D., Goldstein, R., Henly, J. J., Lawrence, D. J., and Shappirio, M., "Deep Space 1 Investigations of Ion Propulsion Plasma Environment," *Journal of Spacecraft and Rockets*, Vol. 37, No. 5, 2000, pp. 545–555.

[9]Richter, I., "FGM Analysis for Deep Space 1, Long Time Data Investigation," Inst. für Geophysik und Meteorologie, Technical Univ. of Braunschweig, Internal Rept. DS1-IGM-TR0004, Germany, Nov. 2000.

[10]Richter, I., Brinza, D. E., Cassel, M., Glassmeier, K. H., Kuhnke, F., Musmann, G., Othmer, C., Schwingenschuh, K., and Tsurutani, B. T., "First Direct Magnetic Field Measurements of an Asteroidal Magnetic Field: DS1 at Braille," *Geophysical Research Letters*, Vol. 28, No. 10, 2001, pp. 1913–1916.

[11]Richter, I., "FGM Analysis for Deep Space 1, The S-Peak Operation," Inst. für Geophysik und Meteorologie, Technical Univ. of Braunschweig, Internal Rept. DS1-IGM-TR0008, Germany, May 2001.